

DEPARTMENT OF PHYSICS

SPACE AND ATMOSPHERIC PHYSICS GROUP

Project code: SPAT-Archer-1

Word count: 8600

---

# Numerically Modelling Magnetopause Surface Waves in Magnetosphere-Ionosphere Coupling

---

*Author:*  
CID: 01702088

*Supervisor:*  
Dr. Martin Archer

*Assessor:*  
Prof. Jonathan Eastwood

A report submitted for the degree of  
*MSci Physics with Theoretical Physics*

April 30, 2023

## Abstract

Global magnetospheric dynamics can be significantly influenced by surface waves on Earth's magnetopause. Due to the limited number of in situ observation points offered by spacecraft, it is preferable to remotely sense these waves using ground-based instruments. Therefore, we employ simplified magnetohydrodynamic theory to numerically model a fundamental mode of the surface wave and predict its main qualitative features expected in ionospheric and ground magnetic observations. Our study indicates that the surface mode has associated field-aligned currents that flow into/out of the ionosphere, leading to an ionospheric potential disturbance and hence the induction of Pedersen and Hall currents in the ionosphere. The field-aligned currents are closed within the ionosphere by the Pedersen currents, while the Hall currents surround the potential source and sink. As a consequence of these current systems, the magnetic field is perturbed, and the total horizontal ground perturbations are approximately oriented in the direction of the field induced by the Hall currents, with the contributions of the Pedersen and the surface mode's currents tending to cancel out. In addition, the ionosphere plays a role in rotating the magnetic field such that the field above it due only to the surface mode is rotated by roughly  $90^\circ$  in comparison to the total field observed on the ground. The parameters in the model are varied and scaling relations between the root-mean-squared magnitudes of the ionospheric currents and the parameters are discovered. For instance, the RMS in both the x and y directions are linearly proportional to the square root of the y-direction wavenumber of the field-aligned currents. The maximum values of the RMS in the x-direction also exhibit a square root relation with the number of periods of the field-aligned currents. Additionally, the RMS of the Hall currents is linearly proportional to the ratio of the ionospheric conductances, whereas the RMS of the Pedersen currents is independent of the conductance. Furthermore, the rotation angle between the horizontal components of the magnetic field measured on the ground and the magnetic field above the ionosphere caused by the surface mode's currents also varies linearly with the conductance ratio. The limitations and implications of the results are discussed, and potential future work is suggested.

### **Acknowledgements**

I want to express my appreciation to my Supervisor for generously sharing his most recent research paper with me and offering constant guidance that helped me complete this project successfully. Additionally, I would like to thank my project partner for the collaboration in sharing the workload and providing encouragement throughout the process.

# Contents

<b>1</b>	<b>Introduction</b>	<b>3</b>
<b>2</b>	<b>Method</b>	<b>7</b>
<b>3</b>	<b>Results</b>	<b>15</b>
3.1	Standard Case . . . . .	15
3.2	Varying parameters . . . . .	17
3.2.1	Varying $N$ . . . . .	17
3.2.2	Varying $k_y$ . . . . .	21
3.2.3	Varying $\Sigma_P$ & $\Sigma_H$ . . . . .	22
<b>4</b>	<b>Conclusion</b>	<b>26</b>
	<b>Bibliography</b>	<b>31</b>

# Chapter 1

## Introduction

The Earth’s geomagnetic field, which extends from the active interior of the Earth to outer space, protects us from the raging solar wind by deflecting those charged particles, forming a well-defined region of space surrounding the Earth known as the magnetosphere. The magnetosphere and its outer boundary, the magnetopause, have been understood to support ultra-low-frequency (ULF) [1] magnetohydrodynamic (MHD) plasma waves, which have wavelengths comparable to the size of the magnetosphere. These ULF waves provide mechanisms for transferring solar wind energy disturbance into the Earth’s geospace, influencing global magnetospheric dynamics and thus space weather’s effects upon us such as magnetosphere-ionosphere (MI) coupling [2], auroral substorms [3] and geomagnetically induced currents (GIC) [4].

The MHD waves can be trapped to form standing waves (i.e. normal modes), which are crucial to interpret a dynamic system. There are three primary MHD waves:

	Propagate along	Driven by	Trapped between	Analogous to
Transverse Alfvén wave	Field lines	Magnetic tension force (field line resonances)	Northern and southern ionospheres	Guitar sting
Fast magnetosonic wave	Radially	Thermal and magnetic pressure gradient	Boundaries within the magnetosphere	Resonating wind chamber
Magnetopause surface wave	Terrestrial magnetic field	Impulsive pressure variations	Northern and southern ionospheres	Drum’s membrane

Table 1.1: Different types of MHD standing waves and their properties. The transverse Alfvén and fast magnetosonic waves are categorized as MHD body waves. The ionosphere refers to the ionized upper layer of the Earth’s atmosphere that faces space. This table is summarised from the paper [5].

So it is natural to think of the Earth’s magnetosphere as a musical instrument and compare the MHD waves to sound waves. In fact, observational studies [6] reveal

that the magnetosphere oscillates at a set of discrete frequencies, known as the 'magic' frequencies (roughly 0.7, 1.3, 1.9, 2.6, ...mHz). The fast magnetosonic waves are radially standing and form cavities and waveguides, leading to so-called global modes, which have been considered as a possible explanation for the 'magic' frequencies [7]. However, this global mode theory fails to reproduce the 'magic' values in regions outside the plasmopause (an inner plasma boundary within the magnetosphere), according to statistical study [8].

Besides the MHD body waves, surface waves can arise due to sharp discontinuities (e.g. magnetopause and plasmopause) that separate plasma regions with different physical parameters. It was stated in [9] that the surface waves can be excited by several processes, both externally (e.g. impulsive solar wind pressure variations, Kelvin-Helmholtz instability) or internally (e.g. drift mirror instability). As with the body waves, the study of surface waves has been based on direct measurements by in-situ spacecraft missions (e.g. THEMIS [10]), simplified mathematical models (e.g. box model magnetosphere [11]) and global MHD simulation codes [12]. In the box model, the magnetopause surface waves are described by a pair of evanescent fast magnetosonic waves (one in each of the half-spaces) that are connected by the boundary conditions at the discontinuity (i.e. magnetopause) [13]. Their eigenmodes of oscillation are referred to as Kruskal-Schwarzschild (KS) modes, named after the two scientists who first predicted the existence of waves propagating along the interface between two distinct plasma regimes [14].

Only recently the direct observational evidence of a magnetopause surface eigenmode (MSE) driven by impulsive pressure variations has been discovered on the dayside magnetosphere, utilising multi-point spacecraft measurements obtained from the THEMIS mission under strict conditions [15]. On the other hand, simulations reveal that the magnetopause surface waves may couple to body waves, leading the entire magnetosphere to oscillate at the MSE's frequencies [5]. Even with a wide range of solar wind conditions, MSE demonstrates frequency preference at 0.7 and 1.15 mHz [16], in good agreement with the first two 'magic' frequencies, indicating that the 'magic' frequencies are likely due to the MSE. These studies imply that MSE is a natural response of the dayside magnetosphere, whose outer boundary can trap surface wave energy resulting in an eigenmode. MSE can serve as a global source of ULF MHD waves and thus play a controlling role in coupling solar wind energy through the Earth's space environment.

However, investigating such a global system response can be challenging with in situ spacecraft measurements and statistical studies [9]. This is because the location of the magnetopause, which is determined by the balance between geomagnetic field and solar wind pressure, changes frequently in response to highly variable solar wind conditions. For a particular event of interest, only a small number of observation points are provided by satellites in the required orbits. Therefore, it would be desirable to remote sense the magnetopause surface waves within the ionosphere or on the ground. Ground-based instruments such as ionospheric radar [17], all-sky imagers [18], and ground magnetometers [1] record near-Earth ULF wave signals, necessitating the need for establishing the ionospheric and ground signatures of MSE so that we can better interpret the data. Auroras, the motion of the ionosphere and

horizontal ground magnetic field perturbations are some of the measurable effects that may be closely related to MSE. Previous work has mainly focused on the body waves, so several open conceptual questions regarding current and magnetic field signatures of the surface waves remain in this field. One would expect the surface wave's signatures to be very different from those of the body waves, as the MSE demonstrates both Alfvén/shear and fast/compressional modes within the magnetopause boundary layer [9, 13].

Some properties of MSE (KS modes) were mathematically established in the simplified box model by Plaschke and Glassmeier [13]. They found that MSE favours a slow solar wind because there is a critical speed (roughly 350km/s) of the shear flow above which no standing MSE can exist. Unlike Alfvén waves, MSE can only be excited at a set of discrete frequencies. The fundamental frequency of the standing MSE was determined to be approximately 0.6 mHz, close to the first 'magic' frequency (and hence the higher ones would be the harmonics). MSE are pure surface waves because the currents supporting these waves only flow within the infinitesimally thin magnetopause boundary, not inside of the two half-spaces. MSE resemble standing Alfvén waves in regions close to the ionosphere. However, in the vicinity of the equatorial plane, MSE are purely compressional. Using solar wind data of one complete solar cycle, the distribution of frequencies of MSE over the full range of solar wind conditions has been established, showing a larger spread in frequency for higher harmonics [19].

It is important to understand how the surface waves' energy couples through the geospace and affects the current and magnetic field signatures in near-Earth regions. When affected by a standing MSE, the northern and southern ionospheres act as the supporting points of the oscillating magnetopause (similar to a drum's membrane). The current associated with the MSE maps into the Earth's ionosphere from high-latitude regions and leads to ionospheric electric potential and field disturbances. As a result, there are ionospheric Pedersen currents, which are created by the ion motion diverted from the  $\mathbf{E} \times \mathbf{B}$  drift due to ion-neutral collisions [20], flowing parallel to the electric field and are thought to provide closure for the MSE's currents feeding into the ionosphere [13] (Because the currents must vanish in the insulating atmosphere located beneath the ionosphere.). Hall effects (due to the presence of the Earth's magnetic field) in the ionosphere allow the electrons continuing the  $\mathbf{E} \times \mathbf{B}$  drift (as electrons are far more mobile than the ions owing to their mass) to produce ionospheric Hall currents perpendicular to the Pedersen currents. The relative amounts of these ionospheric currents are determined by the corresponding height-integrated Pedersen and Hall conductances [20]. These conductances also specify the reflection of MSE between the northern and southern ionospheres and the decay of MSE to other modes [13]. Hence, the Earth's ionosphere plays a key role in controlling the global magnetospheric dynamics and hence the space weather. For example, MSE's energy dissipating in the ionosphere may lead to Joule heating and auroral optical emissions [9].

The direct magnetic field signatures of MSE are also poorly understood. The theory behind magnetic field signatures of ULF waves has focused on either transverse (Alfvén) or fast (compressional) modes, but surface waves (KS modes) are both

Alfvénic and compressional inside the magnetopause boundary layer [9]. The magnetic field signals measured on the ground can be affected by the ionosphere because both the Pedersen and Hall currents perturb the magnetic field [21]. Previous studies indicated that for a plane Alfvén wave, the magnetic field measured on the ground undergoes an exact  $90^\circ$  rotation compared to that above the ionosphere [22]. In contrast, the ground magnetic field signal due to a fast wave is unchanged by the ionosphere because the wave has no currents component flowing into the ionosphere (assuming flat ionosphere and ground) and thus the wave drives no Pedersen and Hall currents [23]. Both transverse and fast modes can couple to one another due to the ionospheric conductivity anisotropy [23]. Hall currents driven by a transverse mode can generate a fast mode and in fact, the ground magnetic field signal is proportional to the Hall currents [22]. For the plane Alfvén waves, one would expect the ground magnetic field to be perfectly aligned with the magnetic field contribution from the Hall currents. However, this is not the case for MSE as shown in [9]. Although MSE (KS mode) is made up of two fast (compressional) waves in each of the two uniform half-spaces, the coupling at the interface (i.e. magnetopause boundary) makes it unique as a fast mode which supports surface currents with components flowing into the ionosphere [9]. Therefore, the ionosphere would not screen the direct effects of MSE from the ground, and the magnetic field can still get rotated.

To further establish the currents and magnetic field features of MSE, we continue the work as in [9] and numerically model an example MSE in a simplified box model magnetosphere. We use a more representative model size and also study how varying parameters in the model influences the results, which has not been done in previous works. As the fundamental (lowest frequency) mode of the magnetosphere oscillation, MSE allows a clearer understanding of how magnetopause surface waves directly impact both the ionosphere and ground, avoiding the complications of coupled effects from other wave modes [9]. This work may provide initial insight for future work in terms of remote sense, auroral activity, Joule heating, MI-coupling, GIC..., as well as modelling surface waves on other magnetospheric boundaries (e.g. plasmapause). We aim to demonstrate the mathematics and computing behind the modelling in detail and discuss the results found in comparison to the literature.



# Chapter 2

## Method

We use the same box model setup as in paper [13], where the magnetospheric signatures of MSE (KS modes) are derived. This is done by straightening the dayside geomagnetic field lines forming a uniform field bounded by the northern and southern ionospheres, as shown in Fig. 2.1.

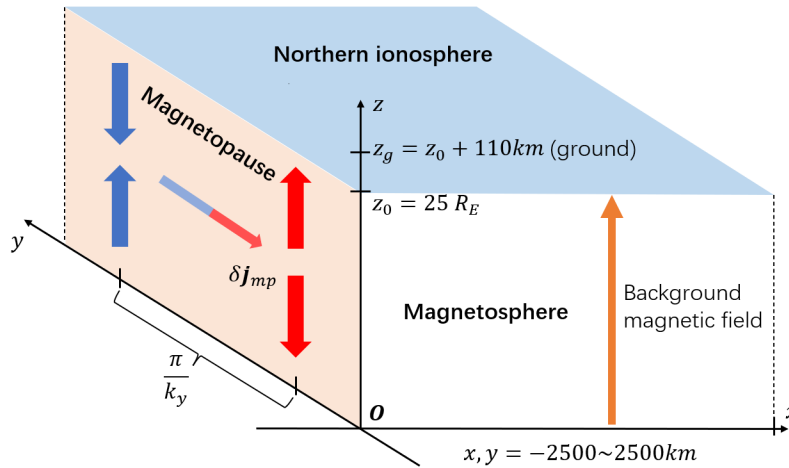


Figure 2.1: Sketch of the box model setup. The northern and southern ionospheres are  $xy$ -planes located at  $z = 25R_E$  and  $z = 0$  respectively, where  $R_E = 6371km$  is the Earth's radius. The half-space with  $x > 0$  represents the magnetosphere, in which the straightened geomagnetic field lines are pointing in the  $z$ -direction. The half-space with  $x < 0$  represents the magnetosheath, in which the geomagnetic field lines are no longer bounded by the ionospheres and may be tilted within the  $yz$ -plane [13]. These two uniform half-spaces with different physical parameters are separated by the  $yz$ -plane of magnetopause discontinuity at  $x = 0$ .

In the following study, we shall focus exclusively on the northern hemisphere. Close to the magnetopause-ionosphere (MI) interface,  $x$  is directed equatorward and  $y$  is directed westward [9]. In each of the two half-spaces, it is assumed that the background electric field and velocity are vanishing, while the background plasma density, pressure, and magnetic field remain constant. In this model, in order to straighten the dayside geomagnetic field lines, we separate the northern and southern hemispheres and flip each of them upside down [24]. So the  $xy$ -plane indicating the ground is located at  $z = 25R_E + 110km$ , where 110km is the altitude of the northern ionosphere with respect to the ground.

The magnetopause and northern ionosphere are modelled as flat rectangular 2D grids. The grid size is determined based on the following criteria. In the z-direction, the same parameters as those used in [9] are adopted in the model. A typical day-side field line length of  $25R_E$  is used, so z ranges from 0 to  $25R_E$ . The z-direction wavenumber is chosen to correspond to the fundamental mode of the surface wave along the field:

$$k_z = 2\pi/50R_E$$

, which gives a wavelength ( $50R_E$ ) twice the size of the magnetosphere. These parameters are maintained constant throughout the simulation because our focus is specifically on the fundamental mode of the surface wave. Azimuthally, the entire pattern will propagate along the y-direction [9]. The current associated with the MSE maps into the ionospheres at high latitude regions. To have a representative scale, we look down to the horizon from the northern ionosphere, which is approximately 110km above the ground, and calculated that the size of the horizon is about 2400km using trigonometry, as shown in Fig. 2.2

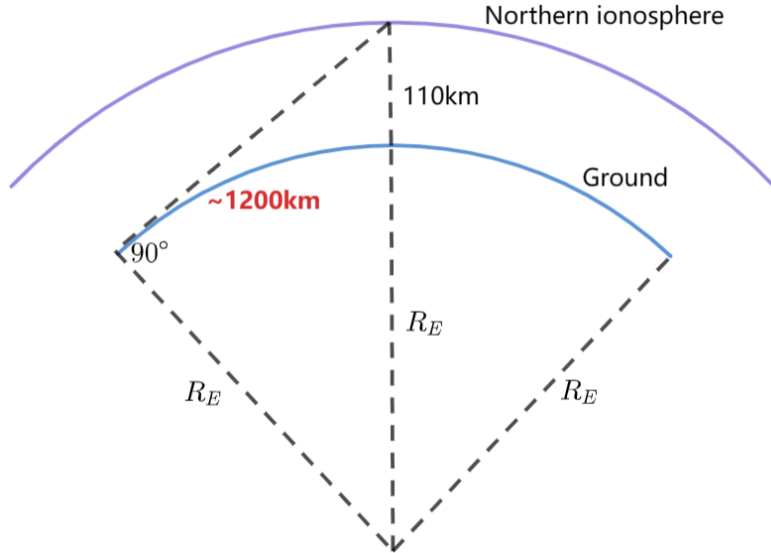


Figure 2.2: Sketch of the geometry of the Earth's high latitude region. A grid with a size comparable to the horizon (blue) and the ionosphere (purple) is desired in order to adequately capture and resolve the ionospheric current and ground magnetic field signatures of MSE in the near-Earth regions of interest, where the ground and ionosphere are considered flat.

Hence the grids are decided to expand from -2500km to +2500km in both x and y-directions, about twice the dimension of the horizon to mitigate potential edge effects [9]. In contrast, a much larger x and y scale of  $10R_E$  was used in [9] to study the signatures of MSE in space at the magnetospheric level, based on previous simulation results. Our study will apply to a single time and therefore use electrostatics, valid since the entire pattern will propagate along y [9]. In the y-direction, there is no need to restrict the wavenumber  $k_y$  because it is a parameter controlling the amount of current mapping into the ionosphere. Besides, we can also vary the number of periods of the current (in y-direction), because the MSE can persist for a few wave periods before decaying away [5].

Plaschke and Glassmeier showed that the currents associated with MSE are confined within the infinitesimally thin magnetopause boundary and bounded by the northern and southern ionospheres [13], which we refer to as the magnetopause currents ( $\delta \mathbf{j}_{mp}(y, z)$ ). Fig. 2.1 roughly demonstrates the magnetopause current system associated with the fundamental MSE (red and blue arrows). These currents are sinusoidal and periodic, and have significant field-aligned components flowing radially into/out of the northern ionosphere at the MI-interface, which we refer to as the field-aligned currents (FAC). In the case of fast magnetosonic waves, the currents flow horizontally, so no FAC is expected [23]. On the other hand, Alfvén waves can lead to FAC, but they are characterized by a volume current system rather than surface currents as with the MSE.

We start with the below expression for the magnetopause current associated with MSE, as derived in [13].

$$\delta \mathbf{j}_{mp}(y, z) = \frac{2\tilde{\tau}}{\mu_0 \rho_{0,b} \Omega_b^2} e^{i(k_y y - \omega t)} \left\{ \begin{pmatrix} k_y k_z \cos(k_z z) \\ -i k_y^2 \sin(k_z z) \end{pmatrix} B_{0,a} \sin \theta_B \right. \\ \left. + \begin{pmatrix} i k_z^2 \sin(k_z z) \\ -k_y k_z \cos(k_z z) \end{pmatrix} [B_{0,a} \cos \theta_B + B_{0,b}] \right\} \quad (2.1)$$

Assuming the background magnetic field in the magnetosheath is parallel to that in the magnetopause (i.e.  $\theta_B = 0$ ), the equation can be considerably simplified [13]. We also drop off those constant proportionality factors describing the plasma and the magnetic field, and take only the imaginary part of the complex exponential to further simplify it. Then the y and z-components that we will use for the magnetopause current are given by

$$\delta \mathbf{j}_{mp}(y, z) = \begin{pmatrix} k_z^2 \sin(k_z z) \cos(k_y y) \\ -k_y k_z \sin(k_y y) \cos(k_z z) \end{pmatrix} \quad (2.2)$$

Following this equation, it is straightforward to show that only the z-component of the magnetopause current that is field parallel remains in the vicinity of the ionospheric plane. The FAC at the MI-interface is defined as the vertical current pointing radially upwards, so it is given by minus the z-component of the magnetopause current:

$$\delta j_r(x, y) = -\delta(x) \delta j_{mp,z}(y, z = z_0) \quad (2.3)$$

, where the use of  $\delta(x)$  indicates that the FAC is confined within the yz-plane of the magnetopause boundary at  $x = 0$ .  $z_0 = 25R_E$  refers to the location of the northern ionosphere in the model. Arbitrary amplitudes (obtained by neglecting those proportionality factors) of quantities (e.g. the FAC) also help ensure calculations remain within floating point precision. By adopting the imaginary part of the complex exponential in the previous step, we obtain a pure sine function that describes the FAC, instead of a cosine function, which ensures a more intuitive anti-symmetrical pattern centred around the origin.

Plaschke and Glassmeier argued that the surface wave's FAC might be closed in the ionospheres by the ionospheric (Pedersen) currents, similar to the case of standing Alfvén waves [13]. However, in their derivations, the ionospheres were assumed

to be infinitely conducting zero-thickness layers, at which the electric field terminates. Hence, we enhance their model by integrating a thin shell ionosphere with finite conductivity [9], taking advantage of the electrostatic MI-coupling method as outlined in [20], applicable due to such low frequencies the surface waves occupy [25]. The ionospheric potential disturbance ( $\delta\psi_{isp}$ ) due to the surface mode's FAC is given by [9, 20]:

$$\begin{aligned}\delta j_r &= \nabla_{\perp} \cdot (\mathbf{\Sigma} \cdot \nabla \delta\psi_{isp})_{\perp} \\ &= \nabla_{\perp} \cdot \left[ \begin{pmatrix} \Sigma_P & -\Sigma_H \\ \Sigma_H & \Sigma_P \end{pmatrix} \cdot \nabla \delta\psi_{isp} \right] \\ &= \Sigma_P \left( \frac{\partial^2}{\partial x^2} + \frac{\partial^2}{\partial y^2} \right) \delta\psi_{isp}\end{aligned}\tag{2.4}$$

, where  $\Sigma_P$  and  $\Sigma_H$  in the conductivity tensor  $\mathbf{\Sigma}$  are the height-integrated ionospheric Pedersen and Hall conductances, both assumed to be uniform throughout the space. This equation applies to the northern hemisphere.  $\delta\psi_{isp}$  at some position  $(x, y)$  on the northern ionosphere is solved numerically by the 2D Green's function for a surface current [9]:

$$\delta\psi_{isp}(x, y) = \iint dx' dy' \frac{\delta j_r(x', y')}{\Sigma_P} \frac{\ln \left( \sqrt{(x - x')^2 + (y - y')^2} \right)}{2\pi}\tag{2.5}$$

Substituting in Eq. 2.3 for the FAC, the 2D integral becomes 1D:

$$\delta\psi_{isp}(x, y) = \frac{1}{2\pi\Sigma_P} \int dy' \left[ -\delta j_{mp,z}(y', z = z_0) \cdot \ln \left( \sqrt{x^2 + (y - y')^2} \right) \right]\tag{2.6}$$

The integral is computed using the trapezium rule at each point  $(x, y)$  on the ionospheric grid. A two-dimensional for loop is used in the code to iterate over all grid positions. The trapezium integration over  $y'$  involves the calculation of the integrand at each grid point with different  $y$  values, and the results are stored as a 1D list. Since the first factor ( $\delta j_{mp,z}(y', z = z_0)$ ) in the integrand only depends on  $y'$ , it is a function of the entire grid, rather than the specific position  $(x, y)$  of interest. Therefore, it is calculated before the loop starts and treated as a constant list of values multiplied by the logarithm. By employing this approach, we avoid the redundant calculations of  $\delta j_{mp,z}(y', z = z_0)$  within the for loop, resulting in a significant saving of computational time. The computation of potential for an ionospheric grid of 1 million points can be completed in about 55 seconds.

Note that the potential cannot be evaluated at the magnetopause discontinuity where  $x = 0$  because this will lead to a  $\ln(0)$  issue while doing the trapezium integration. This intuitively makes sense as the currents feeding into the ionosphere are contained within the magnetopause boundary, where the potential would become infinite. So we adopt an ionospheric grid with uniformly spaced grid points ( $\dots, -1.5\Delta x, -0.5\Delta x, +0.5\Delta x, +1.5\Delta x, \dots$ , similarly in the  $y$ -direction.), excluding the points where  $x = 0$  to compute the potential.

From the potential, the ionospheric electric field is determined through its gradient.

$$\begin{aligned}\delta\mathbf{E} &= -\nabla\delta\psi_{isp} \\ &= -\left(\frac{\partial\delta\psi_{isp}}{\partial x}, \frac{\partial\delta\psi_{isp}}{\partial y}\right)\end{aligned}\quad (2.7)$$

Computationally, this is solved using the finite difference method. For the x-component:

$$\frac{\partial\delta\psi_{ij}}{\partial x} = \frac{\delta\psi_{i,j+1} - \delta\psi_{i,j-1}}{2\Delta x} \quad (2.8)$$

, where the indices  $i$  and  $j$  label the grid points in the  $y$  and  $x$  directions respectively. Similarly, for the  $y$ -component:

$$\frac{\partial\delta\psi_{ij}}{\partial y} = \frac{\delta\psi_{i+1,j} - \delta\psi_{i-1,j}}{2\Delta y} \quad (2.9)$$

These are known as the central difference scheme, valid for the intermediate points. While for the points located at the boundaries of the grid in both directions, a forward/backward difference scheme is used, for example:

$$\frac{\partial\delta\psi_{i0}}{\partial x} = \frac{\delta\psi_{i,1} - \delta\psi_{i,0}}{\Delta x} \quad (2.10)$$

, which calculates the horizontal gradients at the left boundary ( $x = -2500km$ ) of the grid. It does not make sense to evaluate the horizontal gradient across the magnetopause boundary ( $x = 0$ ) where the first derivative of the potential discontinues. So in order to calculate the horizontal gradient at the grid points closest to the magnetopause boundary (i.e. points at  $\pm 0.5\Delta x$ ), we first compute the potential at positions  $\pm 0.25\Delta x$ , and then employ the central difference scheme along with the potential values already evaluated at  $\pm 1.5\Delta x$ . This is done to ensure accurate calculations, as the potential and electric field strength are significant (non-negligible) at these special points. Using the central difference scheme provides a more precise evaluation compared to a forward/backward difference scheme because it takes into account the potential values from both sides of the point of interest. In the  $y$ -direction, there is no such discontinuity that requires additional attention. Two-dimensional for loops are used to iterate over all grid points where  $\delta E_x$  and  $\delta E_y$  are calculated separately.

The ionospheric Pedersen ( $\delta\mathbf{j}_P$ ) and Hall ( $\delta\mathbf{j}_H$ ) currents are determined using Ohm's law [26]:

$$\begin{aligned}\delta\mathbf{j}_\Sigma &= \delta\mathbf{j}_P + \delta\mathbf{j}_H \\ &= \boldsymbol{\Sigma} \cdot \delta\mathbf{E} \\ &= \begin{pmatrix} \Sigma_P & -\Sigma_H \\ \Sigma_H & \Sigma_P \end{pmatrix} \cdot \begin{pmatrix} \delta E_x \\ \delta E_y \end{pmatrix}\end{aligned}\quad (2.11)$$

As previously discussed, the Pedersen and Hall currents are the (electric) field parallel and perpendicular components of the ionospheric currents respectively. Separating from the above equation, we obtain:

$$\delta\mathbf{j}_P = \Sigma_P (\delta E_x, \delta E_y) \quad (2.12)$$

$$\delta \mathbf{j}_H = \Sigma_H (-\delta E_y, \delta E_x) \quad (2.13)$$

Finally, the magnetic field perturbations due to the Pedersen, Hall and magnetopause current systems are calculated separately at position  $\mathbf{r}$ , through Biot-Savart law [21]:

$$\delta \mathbf{B}(\mathbf{r}) = \frac{\mu_0}{4\pi} \iiint d^3 \mathbf{r}' \frac{\delta \mathbf{j}(\mathbf{r}') \times (\mathbf{r} - \mathbf{r}')}{|\mathbf{r} - \mathbf{r}'|^3} \quad (2.14)$$

We first deal with the cross product in the numerator:

$$\begin{aligned} \delta \mathbf{j}(\mathbf{r}') \times (\mathbf{r} - \mathbf{r}') &= \begin{pmatrix} \delta j_x \\ \delta j_y \\ \delta j_z \end{pmatrix} \times \begin{pmatrix} \Delta x \\ \Delta y \\ \Delta z \end{pmatrix} \\ &= \begin{pmatrix} \delta j_y \Delta z - \delta j_z \Delta y \\ -\delta j_x \Delta z + \delta j_z \Delta x \\ \delta j_x \Delta y - \delta j_y \Delta x \end{pmatrix} \end{aligned} \quad (2.15)$$

The magnetic field calculations for Pedersen and Hall currents are similar as they are both confined within the ionospheric xy-plane at  $z_0 = 25R_E$  and therefore can be described using the same set of equations. We introduce a delta function as we did for the FAC to decompose the 3D Biot-Savart integration into 2D:

$$\delta \mathbf{j}(x', y', z') = \delta(z' - z_0) \delta \mathbf{j}(x', y') \quad (2.16)$$

Then the integration along  $z'$  simply yields 1, and sets  $z'$  to  $z_0$  everywhere in the remaining integral. In the cross product (Eq. 2.15),  $\delta j_z$  vanishes as the z-components of Pedersen and Hall currents are both zero. Hence the components of the magnetic field perturbations due to Pedersen or Hall currents are determined by:

$$\delta B_x(x, y, z) = \iint dx' dy' \frac{\delta j_y(x', y') (z - z_0)}{[(x - x')^2 + (y - y')^2 + (z - z_0)^2]^{3/2}} \quad (2.17)$$

$$\delta B_y(x, y, z) = \iint dx' dy' \frac{-\delta j_x(x', y') (z - z_0)}{[(x - x')^2 + (y - y')^2 + (z - z_0)^2]^{3/2}} \quad (2.18)$$

We define  $\Delta z = z - z_0 = h$ , which is the distance from the northern ionospheric plane. The constant factor of  $\mu_0/4\pi$  is ignored. Computationally, these integrals are evaluated using the trapezium rule twice. The logic behind this is using the entire ionospheric grid with known Pedersen/Hall currents to calculate the magnetic field perturbation at some position  $(x, y, z)$ . In the code, this is realized by `trapz[trapz(integrand, y), x]`, where the integrand is computed at each of the grid points and the values are stored as a 2D matrix.

For the magnetopause current system, which is contained within the yz-plane at  $x = 0$ , we employ a similar approach:

$$\delta \mathbf{j}(x', y', z') = \delta(x') \delta \mathbf{j}(y', z') \quad (2.19)$$

As a result,  $x'$  and  $\delta j_x$  are set to 0, leading to the following expressions:

$$\delta B_x(x, y, z) = \iint dy' dz' \frac{\delta j_y(y', z')(z - z') - \delta j_z(y', z')(y - y')}{[x^2 + (y - y')^2 + (z - z')^2]^{3/2}} \quad (2.20)$$

$$\delta B_y(x, y, z) = \iint dy' dz' \frac{\delta j_z(y', z') \cdot x}{[x^2 + (y - y')^2 + (z - z')^2]^{3/2}} \quad (2.21)$$

This work focused exclusively on the horizontal components of the magnetic field perturbations, as it is a measurable quantity that can be characterized in terms of magnitude and rotation angles.

We found that accurately calculating the magnetic field perturbations requires finely resolved grids. So we performed a grid convergence test to determine the right resolution to use. The magnetic field due to the Pedersen current is calculated using the ionospheric grid and the magnetic field due to the magnetopause current is calculated using the magnetopause grid. We calculated these two contributions at a few selected points on the ground ( $z = 25R_E + 110km$ ) and then calculated their root-mean-squared (RMS) magnitude separately. The results obtained at different grid resolutions are summarized in Table 2.1.

Resolution	$\sqrt{\iint  \delta \mathbf{B}_P ^2 dx dy}$	$\sqrt{\iint  \delta \mathbf{B}_{mp} ^2 dx dy}$
$500 \times 500$	1.27155	1.35478
$1000 \times 1000$	1.27152	1.29081
$1600 \times 1600$	1.27152	1.27926

Table 2.1: The RMS values of the horizontal ground magnetic field perturbations due to different current systems. Note that the Pedersen and Hall contributions have identical magnitudes because of the same conductances being used. It is obvious that the calculation of the magnetic field due to the magnetopause current requires a higher resolution of the magnetopause grid. The resolution indicates the number of sample points taken in each direction of the rectangular grid.

We discovered that for the three different resolution choices, the RMS of the Pedersen contribution converges rapidly to a constant value. However, the magnetopause contribution exhibits slight changes with increasing resolution, resulting in an error of less than 1%  $((1.29081 - 1.27926)/1.27926 = 0.0090)$ . Nevertheless, in order to avoid an excessively long computational time, particularly when calculating the Biot-Savart integrations, we ultimately opted for a resolution of  $1000 \times 1000$  (for both grids), which samples the ionosphere and the magnetopause as 1 million uniformly spaced points (with approximately 5km spacing).

There are several parameters that are alterable in the box model. In terms of wave properties, these include the number of FAC periods mapping into the ionosphere ( $N$ ) and the y-direction wavenumber ( $k_y$ ). Additionally, ionospheric properties such as the ionospheric Pedersen ( $\Sigma_P$ ) and Hall ( $\Sigma_H$ ) conductances can also be adjusted.  $k_y$  affects not only the wavelength of the FAC, but also its amplitude, as indicated by

Eq. 2.3. From a different point of view, this can also be explained by the Ampere's Law:

$$\nabla \times \mathbf{B} = \mu_0 \mathbf{j} + \mu_0 \varepsilon_0 \frac{\partial \mathbf{E}}{\partial t} \quad (2.22)$$

By writing the  $\nabla$  in the complex wave representation and ignoring the time-dependent term, we obtain

$$i\mathbf{k} \times \delta \mathbf{B}_0 = \mu_0 \delta \mathbf{j} \quad (2.23)$$

, where  $\delta \mathbf{B}_0$  refers to the constant background magnetic field. Hence, we showed that the magnitude of the current increases with the wavenumber.

The entire project is implemented using Python 3.7 within the scientific environment of Spyder (Anaconda). The main packages employed are numpy, as well as matplotlib for visualisation. The grids are constructed through numpy's meshgrid method, and the integrations are calculated using numpy's trapezium method. The validity of the code was verified by replicating the results presented in [9] using the same parameters. We will first model an example fundamental surface mode with fixed parameters in order to analyze its current and magnetic field signatures. Then we will vary the parameters one at a time to investigate their impacts on the results.



# Chapter 3

## Results

### 3.1 Standard Case

In this section, we provide results for an example fundamental MSE obtained using specific parameters:  $N = 1$ ,  $k_y = 2\pi/2500km$  and  $\Sigma_P = \Sigma_H = 5S$  (valid for sunlit high-latitude regions [9, 20]). We refer to this surface mode with these parameters as the "standard case", as we will be varying parameters in subsequent analyses. Fig. 3.1 demonstrates the surface mode's current system obtained via Eq. 2.2 and Eq. 2.3.

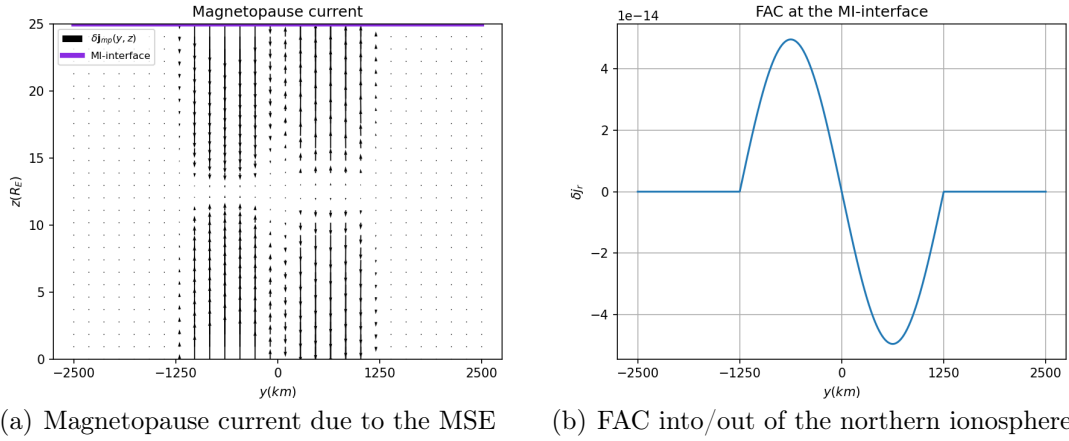


Figure 3.1: Figures of the (standard case) surface mode's current system interacting with the ionospheres. Notably, the box size used in the simulation is twice the dimensions of the currents to minimise potential edge effects. (a) demonstrates the magnetopause currents at selected grid points, revealing the sinusoidal field-aligned components flowing into/out of the northern ionosphere at the MI-interface (hence (b)), which is consistent with Fig.7 in [13].

From the FAC, the associated ionospheric potential, electric field and currents are determined. In Fig. 3.2, the red region represents a potential source where the FAC flows into the ionosphere. Conversely, the blue region represents a potential sink where the FAC flows out of the ionosphere. The Pedersen current flows from the potential source to sink in the East-West direction, providing closure for the FAC as

previously expected. Due to the presence of the Earth’s magnetic field (hence Hall effects), there are Hall currents flowing perpendicular to the Pedersen currents. Their sense of rotation is clockwise surrounding the potential source, and anti-clockwise surrounding the potential sink. The magnitudes of the two currents are identical because of the same conductances used and drop off quickly with distance from the magnetopause boundary at  $x = 0$ .

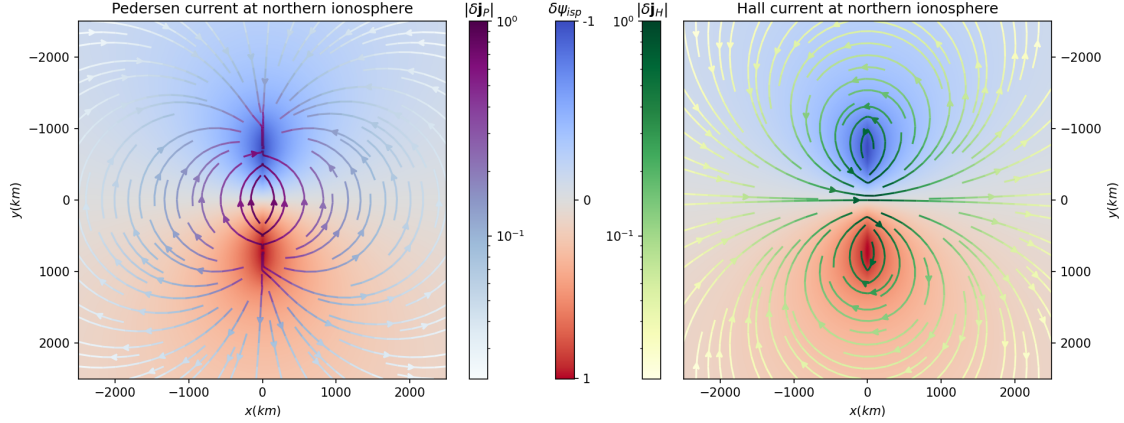


Figure 3.2: Figures showing the streamlines of Pedersen (left) and Hall (right) current patterns at the northern ionosphere, with the potential displayed as a background. The y-axis is inverted so we are looking down on the ionosphere, as this is the convention.

The horizontal ground magnetic field perturbations are computed for each of these current systems. We found that the Pedersen (pink,  $\delta \mathbf{B}_P$ ) and magnetopause (blue,  $\delta \mathbf{B}_{mp}$ ) contributions approximately cancel one another, leading to the total field (black,  $\delta \mathbf{B}_{hor} = \delta \mathbf{B}_{mp} + \delta \mathbf{B}_P + \delta \mathbf{B}_H$ ) points mainly in the direction of the Hall (green,  $\delta \mathbf{B}_H$ ) contribution (see Fig. 3.3). The misalignment from the Hall contribution grows with distance from the magnetopause boundary. These findings contrast significantly with the case of plane Alfvén waves, where we anticipate perfect cancellation of the Pedersen and magnetopause contributions [22], hence the total field would be completely determined by the Hall contribution. This is because the surface wave’s FAC is confined within the infinitesimally thin magnetopause boundary and is bounded by the northern and southern ionospheres, thus does not permeate over space. Notably, the misalignment causes a shift of the total field towards the blue side, whereas in [9] where a much larger model size was used, the shift is more evident and becomes towards the pink side from distance  $\gtrsim R_E$  to the magnetopause boundary.

We now consider the horizontal magnetic fields above the ionosphere due only to the surface wave’s currents (i.e. magnetopause currents), which are shown as the deep blue arrows in Fig. 3.4, evaluated at  $400km$  altitudes (or  $h = 110km - 400km = -290km$  equivalently). The magnetic field due to plane Alfvén waves must be seen rotated exactly by  $90^\circ$  when observed on the ground [22]. However, we discovered that this is not the case for surface waves. As depicted by the colour map, the angles between the deep blue and ground black arrows (i.e. total perturbations) deviate from  $90^\circ$ , especially close to the magnetopause boundary at  $x = 0$ . This is due to

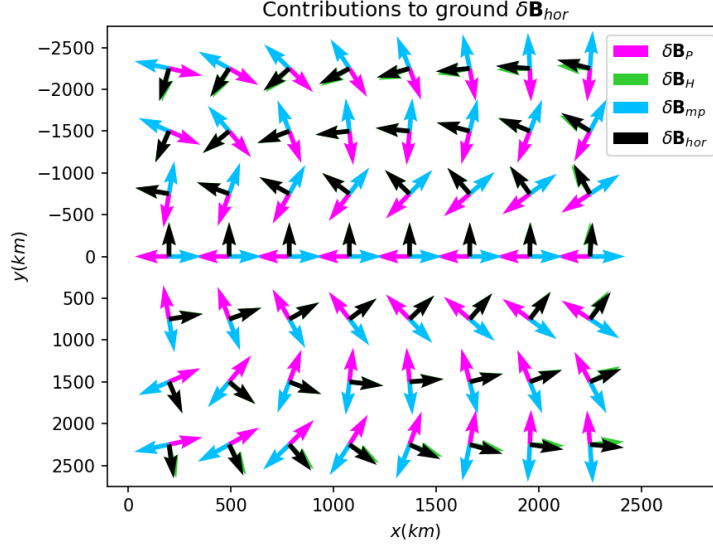


Figure 3.3: Vector plot illustrating the contributions to the horizontal ground magnetic field due to different current systems at a few selected positions with positive  $x$ . The ground refers to an  $xy$ -plane located at zero altitude, with a distance of  $h = 110\text{km}$  to the northern ionosphere and thus a coordinate of  $z = 25R_E + 110\text{km}$  in the model. The coloured arrows in the plot are normalized to the black arrow, which is set to 1 at each position shown. These arrows are of comparable size and exhibit patterns that are somewhat similar to the currents.

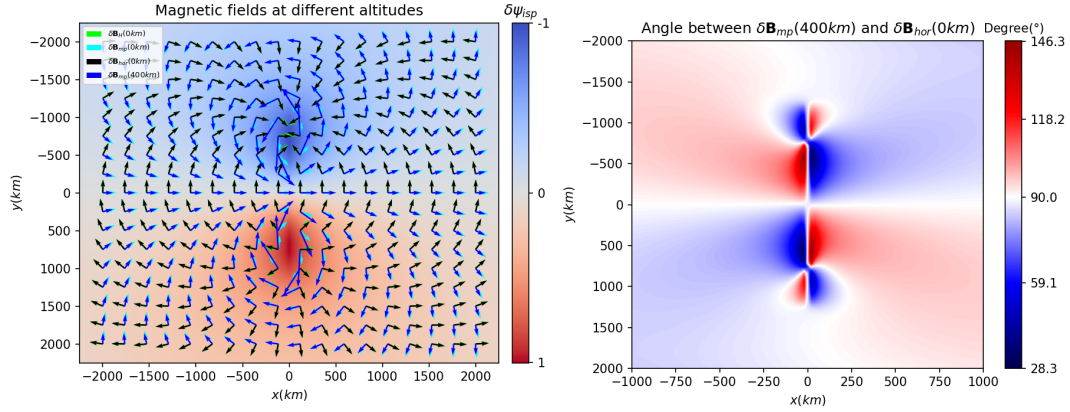
the non-cancellation of the magnetopause and Pedersen contributions on the ground. Furthermore, there is only a slight displacement in the  $\delta\mathbf{B}_{mp}$  above and below the ionosphere, as evidenced by the light blue arrows in the figure, indicating that it is less sensitive to altitudes. Therefore, the ionosphere plays a key role in rotating the magnetic field above it due solely to the surface wave through the perturbations caused by the ionospheric currents.

## 3.2 Varying parameters

This section of the study is motivated by [9] in which research similar to the previous section was conducted. The paper stated that varying certain parameters would produce qualitatively similar outcomes, but the full parameterisation was reserved for future work. Therefore, in the following section, we will be adjusting individual parameters within the model to quantitatively analyse their impacts on the currents and magnetic fields.

### 3.2.1 Varying $N$

According to previous studies, MSE can persist for a few wave periods [5]. Since the entire pattern would propagate azimuthally [9], it is possible to have multiple periods of FAC being mapped into the ionosphere at a single time. We limit the  $N$  values between 1 and 5, as too many periods would be unrealistic, and maintain  $k_y = 2\pi/(625\text{km})$  and  $\Sigma_P = \Sigma_H = 5S$  constant. We opted for a  $k_y$  value that



(a) Magnetic fields above and below ionosphere (b) Rotation of magnetic fields by ionosphere

Figure 3.4: Figures showing the rotation of horizontal magnetic fields by the ionosphere. In (a), The magnetopause contributions (blues) have a similar sense of rotation as Hall currents surrounding the potential source and sink, whereas the total fields (black) flow approximately parallel to the Pedersen currents. The coloured arrows are normalised to the black arrows. Colour map (b) shows the angle of rotation between the deep blue and black arrows, calculated via  $\cos \theta = (\delta \mathbf{B}_{mp} \cdot \delta \mathbf{B}_{hor}) / |\delta \mathbf{B}_{mp}| |\delta \mathbf{B}_{hor}|$ , illustrating a centrosymmetric pattern of the distribution of the angles. Further away from the magnetopause boundary ( $x = 0$ ) and on the axes, the angle approaches  $90^\circ$ .

ensures the box size is considerably larger than the FAC size (no matter what value  $N$  takes), thus minimizing the potential edge effects.

Varying  $N$  has an immediate effect on ionospheric potential and current patterns. Fig. 3.5 demonstrates the results obtained with two FAC periods ( $N = 2$ ). Interestingly, the strength of the potential reaches its maximum values at both ends where the FAC peaks, rather than the middle. The Pedersen currents continue to close the FAC flowing into or out of the ionosphere. For example, it establishes a connection between a potential source (red) and the neighbouring potential sink (blue), as well as with the distant potential sink on a significantly larger scale.

We calculated the root-mean-squared magnitude (RMS) of the ionospheric electric field, currents, as well as magnetic field perturbations, and investigated how they change with the varying parameters. For example, the RMS of Pedersen currents can be determined by

$$RMS_{x,y} = \sqrt{\int (\delta j_{P,x}^2 + \delta j_{P,y}^2) dy, x} \quad (3.1)$$

It can be computed along either  $x$  or  $y$  direction, using the trapezium rule. Because of the identical Pedersen and Hall conductances used, the RMS of the Pedersen and Hall currents are also identical, and the RMS of the electric field differs only by a constant factor of  $\Sigma_P$ . Fig. 3.6 displays at different  $N$  values the RMS of the Pedersen/Hall currents evaluated along  $x$  and  $y$  directions respectively. In the  $x$ -direction, the RMS maximises at the magnetopause discontinuity ( $x = 0$ ) and rises

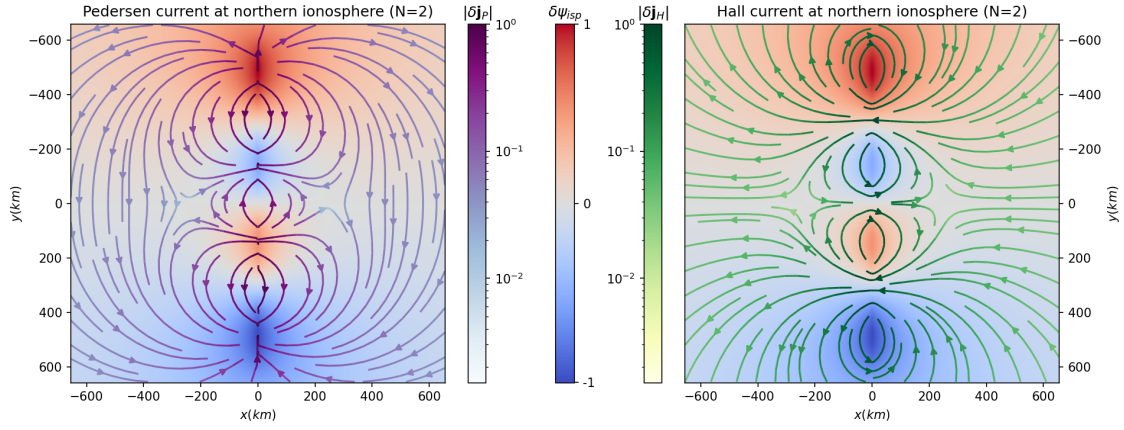


Figure 3.5: Ionospheric potential and current patterns resulted from FAC with  $N = 2$ . We zoom into the centre of the ionospheric grid ( $600\text{km} \times 600\text{km}$ ) to capture the details of the patterns that are different from the  $N = 1$  case.

with increasing  $N$  values, possibly due to the increased amount of currents mapping into the ionosphere. On the other hand, in the  $y$ -direction, for cases with  $N > 1$ , the RMS peaks occur at both ends where the electric potential vanishes (see Fig. 3.5), rather than the middle. Additionally, as  $N$  increases, the RMS curves expand to cover a larger  $y$ -directional region.

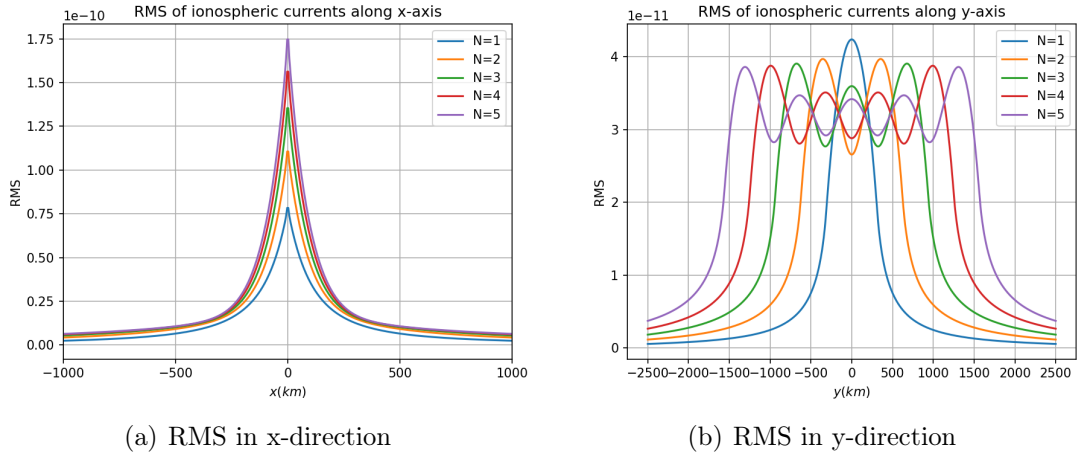


Figure 3.6: The RMS of ionospheric currents assessed with varying  $N$  values. The  $x$ -direction RMS is determined by integrating the 2D matrix that stores the squared magnitudes of the current along the  $y$ -direction, which yields a 1D list of values. Similarly for the  $y$ -direction RMS. The  $x$ -direction RMS exhibits a discontinuity at the magnetopause boundary ( $x=0$ ) in its first derivative, whereas the  $y$ -direction RMS displays smooth behaviour at this location.

It is important to know whether scaling relations exist for the RMS with  $N$ . To explore this, we begin by examining the maximum values of the RMS in both the  $x$  and  $y$  directions. Our findings (see Fig. 3.7) indicate that the maximum values of the  $x$ -direction RMS follow a square root relation with  $N$ , while the maximum

values of the y-direction RMS follow a relation where  $N$  is lowered to the power of -1.50. The power of  $N$  ( $p$ ) and the coefficients  $a$  and  $b$  are determined through fitting procedures. Notably, in the x-direction, given that  $a$  is close to 1 and  $b$  is negligible, it can be inferred that the maximum values of the x-direction RMS are linearly proportional to the square root of  $N$ , with a fitted value of the power being almost equal to 0.5.

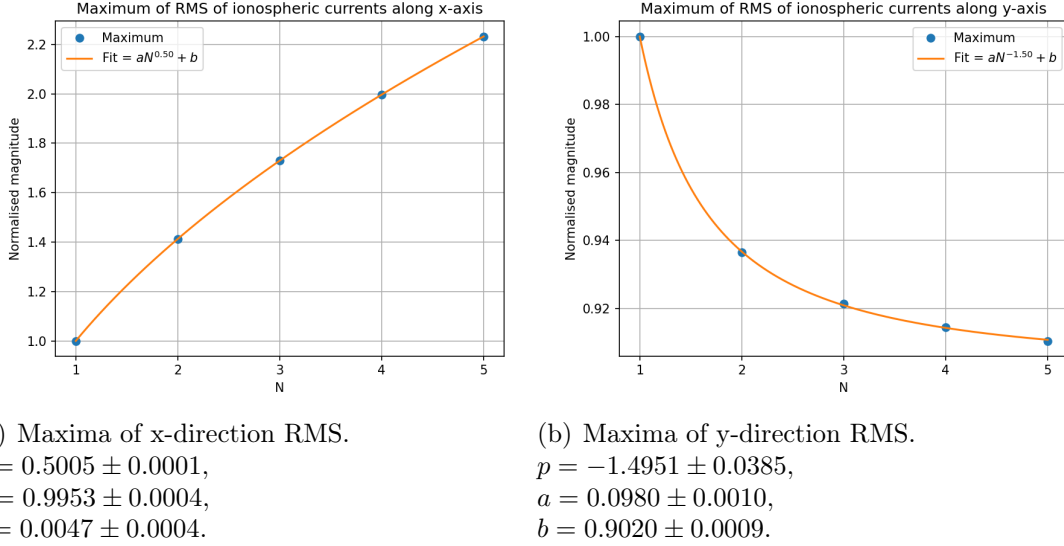


Figure 3.7: The maximum values of the RMS in both directions. The curve fit method was applied to discover the scaling relations and determine the fitting coefficients whose errors are evaluated by the square root of the diagonal values of the corresponding covariance matrix.

Given the similarity in the shape of those curves shown in Fig. 3.6 (a), an important question to address is whether the square root scaling relation applies uniformly along the entire x-axis. To investigate this, the RMS values are divided by the square root of the corresponding  $N$  value and plotted against  $k_y x$ , as shown in Fig. 3.8. We observed that the curves fall on top of one another in the region very close to the magnetopause boundary. However, further away from this region, the curves no longer overlap. Therefore, we conclude that the square root scaling relation holds only in the vicinity of the magnetopause boundary, where the x-direction RMS values maximise.

$$\text{Max}[RMS_x(N)] \propto \sqrt{N} \quad (3.2)$$

$$\text{Max}[RMS_y(N)] = aN^{-1.50} + b \quad (3.3)$$

Efforts were made to employ similar techniques to determine scaling relations for magnetic field perturbations. However, no obvious scaling relation could be found for the magnetic fields. One probable explanation for this is that the computation of the Biot-Savart integration is excessively time-consuming, which necessitated us



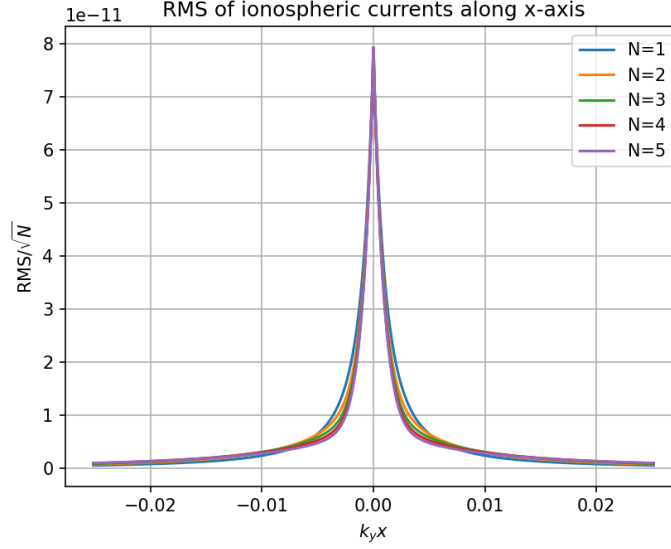


Figure 3.8: Plot of the x-direction RMS curves with both axes scaled. Perfect overlapping of the curves would be expected if the square root scaling relation is valid throughout the x-direction.

to reduce the number of points at which magnetic fields were calculated. Consequently, it may not have been able to accurately evaluate the RMS of the magnetic fields. Alternatively, it could be because the magnetic fields are calculated from the currents, which do exhibit scaling relations, and the Biot-Savart law may have introduced additional complexity to the mathematics.

Finally, how varying  $N$  affects the total horizontal ground magnetic field perturbations was qualitatively investigated. As illustrated in Fig. 3.9, for  $y > 0$ , the direction of the fields undergoes an anti-clockwise shift as  $N$  increases, while for  $y < 0$ , the shift is clockwise. The magnitude of the shift becomes smaller as the distance from the magnetopause boundary ( $x = 0$ ) increases. The direction remains unchanged on the y-axis ( $y = 0$ ).

### 3.2.2 Varying $k_y$

In this section,  $N = 1$ ,  $\Sigma_P = \Sigma_H = 5S$  and different  $k_y$  values are generated using the formula

$$k_y = 2\pi / (625km \times (\sqrt{2})^a)$$

, where  $a$  is an integer ranging from 0 to 4. When  $a = 4$ ,  $k_y = 2\pi/2500km$ , which produces exactly the standard case (i.e. FAC size = half box size). Increasing the value of  $k_y$  results in an increase in the FAC amplitude but a decrease in the FAC wavelength. The ionospheric potential and current patterns obtained at different  $k_y$  values are qualitatively similar in terms of their shapes. One obvious difference is that the separation between the potential source and sink becomes larger as  $k_y$  decreases, leading the currents to flow over much larger scales.

Following similar procedures as in the previous section, it was revealed that the

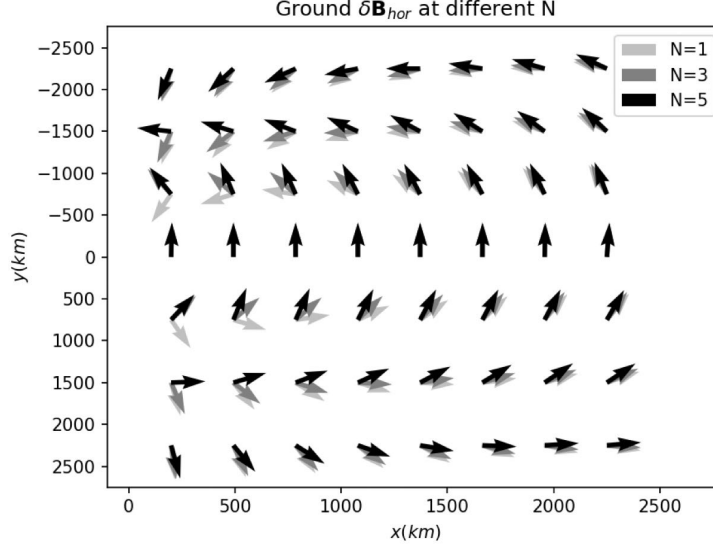


Figure 3.9: Horizontal ground magnetic field perturbations evaluated at different  $N$  values.  $\delta\mathbf{B}_{\text{hor}} = \delta\mathbf{B}_{mp} + \delta\mathbf{B}_P + \delta\mathbf{B}_H$ . All of the arrows are normalised to 1.

RMS of the ionospheric currents (as well as the electric field) scales proportionally to the square root of  $k_y$ . This scaling relation applies in both  $x$  and  $y$  directions and holds not just for the maximum values, but generally along the entire  $x$  and  $y$  axes scaled by  $k_y$ . As an example, Fig. 3.10 (a) illustrates the  $y$ -direction RMS curves that were obtained at various  $k_y$  values. Then the vertical axes are scaled by the square root of  $k_y$  and plotted against  $k_y y$  as shown in (b). We observed that the curves perfectly fall on top of one another, indicating that the scaling relation holds true throughout the axis in the range of  $k_y y$ .

$$RMS(k_y) \propto \sqrt{k_y} \quad (3.4)$$

The qualitative dependence of the total horizontal ground magnetic field perturbations upon the values of  $k_y$  is illustrated in Fig. 3.11, which exhibits a comparable trend to that observed when  $N$  is adjusted. However, the shift of the arrows when  $k_y$  is being varied is less obvious.

### 3.2.3 Varying $\Sigma_P$ & $\Sigma_H$

Finally, we modified the two ionospheric conductances and analyse their impacts mathematically. The expression of the ionospheric potential (see Eq. 2.6) includes a factor of  $\Sigma_P$  in the denominator. As the integral depends solely on the entire ionospheric grid, it can be regarded as a constant. Hence we can extract the  $1/\Sigma_P$  factor, which then propagates throughout the calculation. The electric field is the gradient of the potential (see Eq. 2.7), so it also scales with  $1/\Sigma_P$ . As for the Pedersen current, the  $\Sigma_P$  factor in its own expression (see Eq. 2.12) cancels the one from the potential, making it independent of the conductances. And for the Hall current, the  $\Sigma_H$  in its own expression (see Eq. 2.13) makes it scale with the conductance ratio



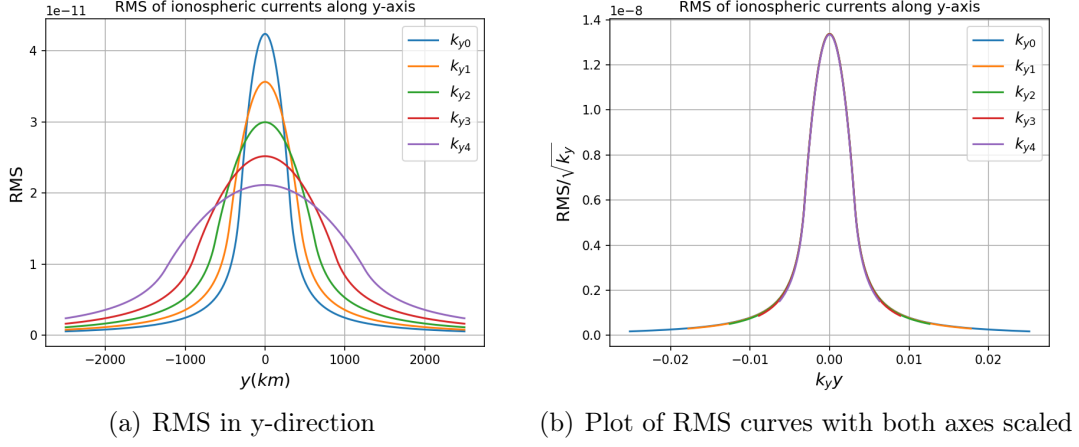


Figure 3.10: Plots depicting the y-direction RMS of Pedersen/Hall currents.  $k_{y0}$  represents the largest  $k_y$  value obtained with  $a = 0$ , which leads to the smallest FAC wavelength but the largest FAC amplitude. Hence the  $k_{y0}$  curve is the narrowest but tallest one. Since  $N = 1$  is used, these y-direction RMS curves all feature a single peak. After scaling the horizontal axis as  $k_y y$ , all curves possess an identical shape.

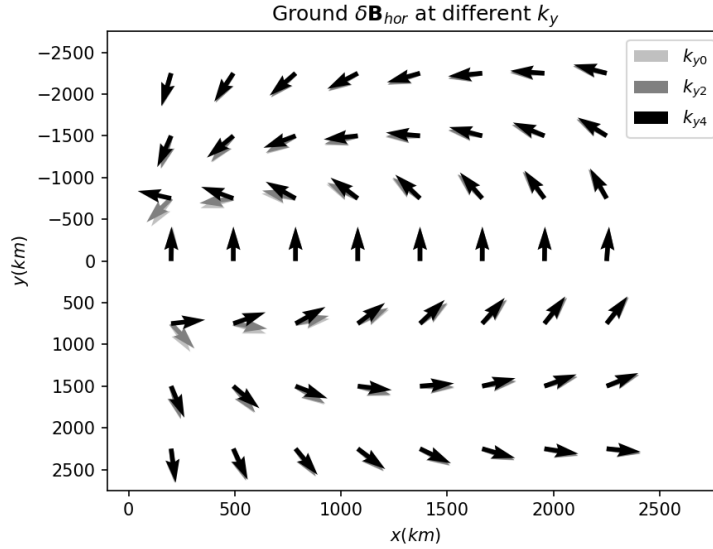


Figure 3.11: Horizontal ground magnetic field perturbations evaluated at different  $k_y$  values.  $\delta \mathbf{B}_{\text{hor}} = \delta \mathbf{B}_{mp} + \delta \mathbf{B}_P + \delta \mathbf{B}_H$ . All of the arrows are normalised to 1.

$\Sigma_H/\Sigma_P$ . Furthermore, according to Eq. 2.14, no extra conductance dependence is introduced by the Biot-Savart integrations. Therefore, the magnetic field perturbation due to the Pedersen currents (as well as the magnetopause currents) is also independent of the conductances and that due to the Hall currents depends linearly upon the conductance ratio. These scaling relations should also be applicable to the RMS of the above quantities because the RMS does not change the dimensionality of a quantity. Additionally, these relations hold uniformly in both the x and y directions since the mathematical derivations are valid at all positions.

$$RMS(\delta \mathbf{E}) \propto \frac{1}{\Sigma_P} \quad (3.5)$$

$$RMS(\delta \mathbf{j}_P) \propto 1 \quad (3.6)$$

$$RMS(\delta \mathbf{j}_H) \propto \frac{\Sigma_H}{\Sigma_P} \quad (3.7)$$

The above conjecture about scaling relations is verified through plotting, as was done previously for N and  $k_y$ . We use  $N = 1$  and  $k_y = 2\pi/2500km$  as with the standard case. We present the x-direction RMS of Hall currents evaluated at multiple values of the conductance ratio as an example (see Fig. 3.12 (a)). We vary both conductances to obtain the conductance ratios to maintain generality. Fig. 3.12 (b) depicts that the maximum values of the RMS curves are linearly proportional to the conductance ratio. Dividing the RMS values by the corresponding conductance ratio results in the overlapping of the curves throughout the entire x-axis as expected.

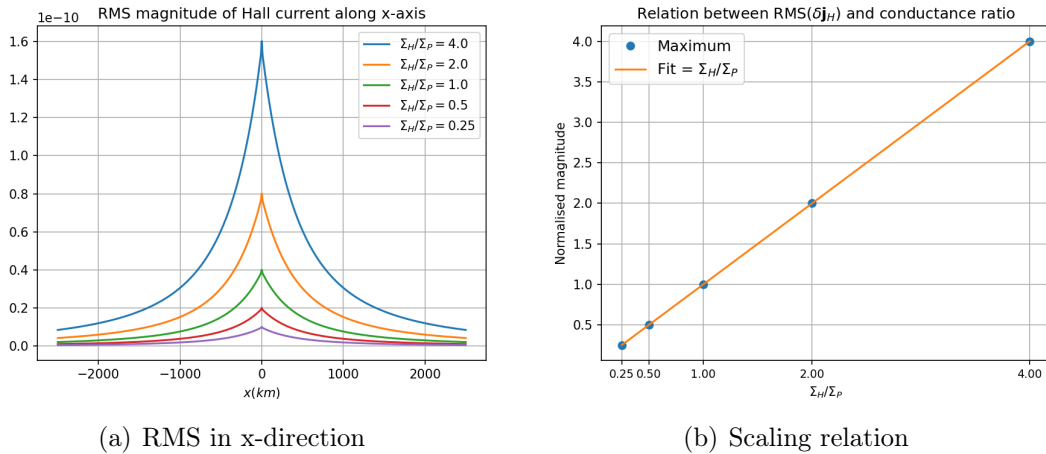


Figure 3.12: Figure showing the x-direction RMS curves of Hall currents obtained at various values of the conductance ratio, along with the scaling relation determined through the fitting, which implies a linear relationship between the maximum values of the RMS and the conductance ratio.

We now return to consider how varying conductances would affect the rotation angle between the horizontal components of the magnetic field perturbations above the

ionosphere due only to the magnetopause currents (deep blue arrows, as in Fig. 3.4 (a)) and the total ground perturbations (black). As previously discussed, the magnetic fields due to Pedersen currents and magnetopause currents are unchanged by the conductances, while the magnetic field due to Hall currents is linearly proportional to  $\Sigma_H/\Sigma_P$ . Therefore, when  $\Sigma_H$  increases (or  $\Sigma_P$  decreases), the Hall contribution (green) becomes larger, causing the total field (black) shifts towards the green side (i.e. away from the blue side). Since the blue arrows maintain unchanged, the rotation angle between the deep blue and black arrows would thus become larger. The distributions of rotation angles obtained at different values of  $\Sigma_H$  are shown in Fig. 3.13, from which we can see a slight increase in the values of the rotation angles as  $\Sigma_H$  becomes larger. A contrary trend can be observed for increasing  $\Sigma_P$ .

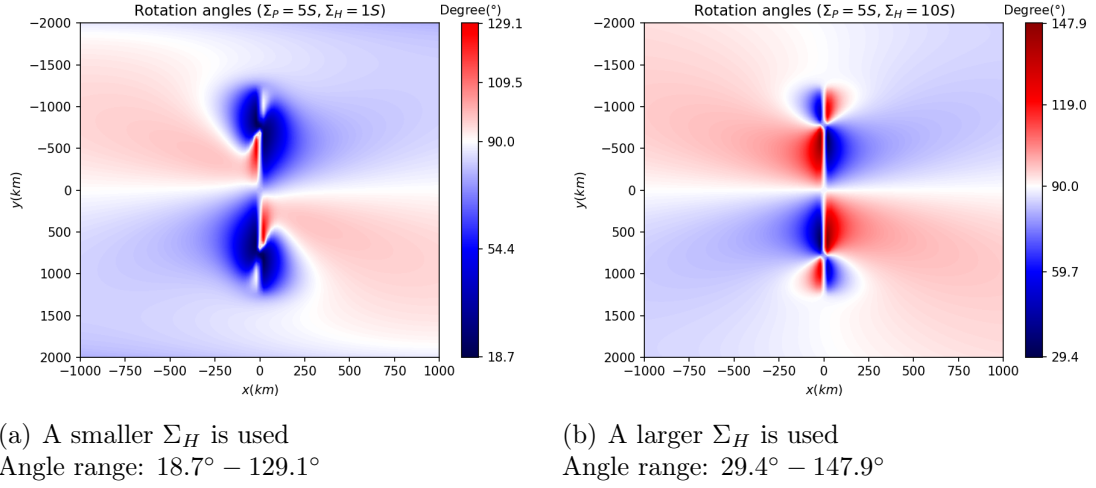


Figure 3.13: Distributions of the angles between  $\delta \mathbf{B}_{mp}(400km)$  and  $\delta \mathbf{B}_{hor}(0km)$  obtained at  $\Sigma_H = 1S$  and  $\Sigma_H = 10S$ .  $\Sigma_P$  is kept constant. When  $\Sigma_H = 5S$  (the standard case), the angle range is  $28.3^\circ - 146.3^\circ$ , as shown in Fig. 3.4 (b). There is an evident increase in the values of the rotation angles as  $\Sigma_H$  becomes larger. Furthermore, the distribution becomes more centred around  $90^\circ$ .

# Chapter 4

## Conclusion

MHD theory has been utilized to study the direct effects of magnetopause surface waves on the features of ionospheric currents and ground magnetic fields. An example of fundamental surface mode has been numerically modelled in a simplified box model magnetosphere through computational methods. The key findings of our study are as follows:

Magnetopause surface modes have associated FAC flowing into/out of the ionosphere at the magnetopause-ionosphere interface. These currents result in an ionospheric potential disturbance which drives Pedersen and Hall currents, whose magnitudes become smaller as the distance from the magnetopause increases. The Pedersen currents provide closure for the FAC, while the Hall currents, which are perpendicular to the Pedersen currents, surround the potential source and sink. All these current systems contribute to magnetic field perturbations according to the Biot-Savart law. On the ground, the total horizontal magnetic fields are approximately aligned with the fields induced by the Hall currents. The misalignments are caused by the fact that the Pedersen and magnetopause contributions do not perfectly cancel one another, controverting the case with the plane Alfvén waves. The horizontal field measured on the ground is rotated by approximately  $90^\circ$  compared to that above the ionosphere due only to the surface wave's currents, except in regions close to the magnetopause boundary. These findings are qualitatively similar to those presented in [9], where a much larger model size was used. The current and magnetic field patterns will slightly change if the parameters in the model are adjusted.

The root-mean-squared (RMS) magnitudes of the ionospheric electric field and currents are calculated using different parameters and scaling relations with respect to the parameters are discovered. For varying  $N$ , the maximum values of the RMS in the x-direction exhibit an obvious square root relation with  $N$ , while in the y-direction, the maximum values obey an equation in which  $N$  is to the power of -1.50. For varying  $k_y$ , a square root relation that applies uniformly in both directions was found. Finally, for varying the conductances, each quantity scales differently and the relations were determined mathematically. Tab. 4.1 summarises these scaling relations. No obvious scaling relations could be found for the magnetic field perturbations due to the limitation of computational power or the fact that there may not exist scaling relations at all. In addition to the scaling relations, it was revealed that the rotation angles between the horizontal components of the magnetic field

measured on the ground and the magnetic field above the ionosphere due only to the surface mode increase as the Hall conductance increases or the Pedersen conductance decreases.

	$RMS(\delta \mathbf{E})$	$RMS(\delta \mathbf{j}_P)$	$RMS(\delta \mathbf{j}_H)$
$k_y$	$\propto \sqrt{k_y}$		
$N$	x-direction maximum: $\propto \sqrt{N}$ y-direction maximum: $aN^{-1.50} + b$		
$\Sigma_{P,H}$	$\propto 1/\Sigma_P$	Constant	$\propto \Sigma_H/\Sigma_P$

Table 4.1: A summary of the scaling relations found, indicating how the ionospheric quantities change with the parameters in the model.

We briefly discuss the implications of the results. Since it is most desirable to remotely sense the magnetopause surface waves within the Earth’s environment, our results would help interpret the signals captured by the ground-based instruments. For instance, by measuring the Doppler shift of the reflected radio waves, ionospheric radars [17] can provide information about the direction and velocity of the plasma motion within the ionosphere. The ionospheric velocity is determined by the  $\mathbf{E} \times \mathbf{B}$  drift. Since  $\mathbf{B}$  (background field) is roughly constant, the ionospheric velocity is directly proportional to the ionospheric electric field, whose scaling relations with respect to the parameters have been revealed. Therefore, it would be possible to detect the surface waves’ impacts on the ionospheric velocity through radar measurements. On the other hand, ground magnetometers [27] monitor the change in the strength and direction of the Earth’s magnetic fields over time, and thus would record signals attributed to the magnetopause surface waves. Understanding the direct magnetic field signatures of the surface modes, as well as how they vary with the parameters would therefore be helpful in finding evidence of the surface modes from the data taken by the magnetometers. From the ground-based data, along with the scaling relations found, one would be able to predict the properties of a detected surface mode in terms of the associated current ( $N$  &  $k_y$ ), and the state of the ionosphere ( $\Sigma_{P,H}$ ) at the time of detection.

Besides the remote sense, the surface modes may be closely related to space weather processes such as Joule heating, aurorae and geomagnetically induced currents. Surface modes’ energy may dissipate in the ionosphere and is consumed by Joule heating (due to Pedersen currents) and auroral optical emissions [28]. The observed auroral patterns have been considered the results of the ULF waves. For example, it has been suggested in [9] that the surface modes’ upward FAC may lead to periodic auroral brightenings. In addition, paper [9] also indicated that surface modes could generate oscillatory magnetic fields on the Earth’s surface, which may lead to geomagnetically induced currents driven by geoelectric fields. Hence understanding how the ionospheric currents and ground magnetic fields due to surface modes change with the wave’s and ionospheric properties would improve our prediction of these phenomena as well as potential space weather hazards.

However, there are limitations to the results due to the use of the simplified box model. First of all, straightening the dayside geomagnetic field lines can only be

an imprecise approximation of reality, especially close to the cusp/polar regions where the geomagnetic field lines are highly curved [13]. Besides, the northern and southern ionospheres are treated as separate entities, while in reality they should be interconnected. Moreover, the simplified box model assumes that both the ionospheres and the magnetopause are flat planes. However, paper [9] introduced a finite thickness magnetopause boundary and demonstrated that the FAC associated with surface modes maximises at the inner/equatorward edge of the magnetopause boundary layer, rather than the open-closed boundary (the boundary at which the geomagnetic field lines transition from being closed to open [29], confined within the magnetopause layer) as previously considered. Consequently, the assumption of infinitesimally thin boundaries may fail to fully capture the underlying physics. In addition, the parameters (e.g. ionospheric conductances) are assumed to be uniform throughout space and remain constant over time, which is unrealistic given the frequently changing conditions of the solar wind. MHD box models are an effective way to gain useful preliminary insights. Global simulations should be employed to enhance the understanding.

For future studies, one could further investigate the magnetic field due to individual current systems as well as the total field because how their magnitudes quantitatively vary with the parameters is still unclear due to the limitation of computational time. Additionally, the changes in the magnetic fields with altitude in terms of both the strength and rotation angles could be explored. It would be beneficial to incorporate the vertical components of the fields to gain a more complete understanding. Besides the magnetic fields, similar work could be carried out for higher harmonics of the magnetopause surface modes, as well as for the surface waves present on other boundaries within the magnetosphere such as the plasmopause.

# Bibliography

- [1] J. A. Jacobs, Y. Kato, S. Matsushita, and V. A. Troitskaya. Classification of geomagnetic micropulsations. *Journal of Geophysical Research*, 69(1):180–181, 1964.
- [2] Andreas Keiling. Alfvén waves and their roles in the dynamics of the earth’s magnetotail: A review. *Space Science Reviews*, 142(1-4):73–156, 2008.
- [3] Larry Kepko and Margaret Kivelson. Generation of pi2 pulsations by bursty bulk flows. *Journal of Geophysical Research: Space Physics*, 104(A11):25021–25034, 1999.
- [4] M. J. Heyns, S. I. Lotz, and C. T. Gaunt. Geomagnetic pulsations driving geomagnetically induced currents. *Space Weather*, 19(2), 2021.
- [5] M. O. Archer, M. D. Hartinger, F. Plaschke, D. J. Southwood, and L. Rastaetter. Magnetopause ripples going against the flow form azimuthally stationary surface waves. *Nature Communications*, 12(1), 2021.
- [6] J. C. Samson, B. G. Harrold, J. M. Ruohoniemi, R. A. Greenwald, and A. D. Walker. Field line resonances associated with mhd waveguides in the magnetosphere. *Geophysical Research Letters*, 19(5):441–444, 1992.
- [7] Margaret G. Kivelson and David J. Southwood. Coupling of global magnetospheric mhd eigenmodes to field line resonances. *Journal of Geophysical Research*, 91(A4):4345, 1986.
- [8] M. D. Hartinger, V. Angelopoulos, M. B. Moldwin, K. Takahashi, and L. B. Clausen. Statistical study of global modes outside the plasmasphere. *Journal of Geophysical Research: Space Physics*, 118(2):804–822, 2013.
- [9] M. O. Archer, M. D. Hartinger, L. Rastätter, D. J. Southwood, M. Heyns, J. W. Eggington, A. N. Wright, F. Plaschke, and X. Shi. Auroral, ionospheric and ground magnetic signatures of magnetopause surface modes. *Journal of Geophysical Research: Space Physics*, 128(3), 2023.
- [10] V. Angelopoulos. The themis mission. *The THEMIS Mission*, page 5–34, 2009.
- [11] D.J. Southwood. Some features of field line resonances in the magnetosphere. *Planetary and Space Science*, 22(3):483–491, 1974.
- [12] M. D. Hartinger, F. Plaschke, M. O. Archer, D. T. Welling, M. B. Moldwin, and A. Ridley. The global structure and time evolution of dayside magnetopause surface eigenmodes. *Geophysical Research Letters*, 42(8):2594–2602, 2015.

- [13] F. Plaschke and K.-H. Glassmeier. Properties of standing kruskal-schwarzschild-modes at the magnetopause. *Annales Geophysicae*, 29(10):1793–1807, 2011.
- [14] M Kruskal and M Schwarzschild. Some instabilities of a completely ionized plasma. *Proceedings of the Royal Society of London. Series A. Mathematical and Physical Sciences*, 223(1154):348–360, 1954.
- [15] M. O. Archer, H. Hietala, M. D. Hartinger, F. Plaschke, and V. Angelopoulos. Direct observations of a surface eigenmode of the dayside magnetopause. *Nature Communications*, 10(1), 2019.
- [16] M. O. Archer, M. D. Hartinger, and T. S. Horbury. Magnetospheric “magic” frequencies as magnetopause surface eigenmodes. *Geophysical Research Letters*, 40(19):5003–5008, 2013.
- [17] A.D.M. Walker, R.A. Greenwald, W.F. Stuart, and C.A. Green. Stare auroral radar observations of pc 5 geomagnetic pulsations. *Journal of Geophysical Research*, 84(A7):3373, 1979.
- [18] Eric Donovan, Stephen Mende, Brian Jackel, Harald Frey, Mikko Syrjäso, Igor Voronkov, Trond Trondsen, Laura Peticolas, Vassilis Angelopoulos, Stewart Harris, and et al. The themis all-sky imaging array—system design and initial results from the prototype imager. *Journal of Atmospheric and Solar-Terrestrial Physics*, 68(13):1472–1487, 2006.
- [19] M. O. Archer and F. Plaschke. What frequencies of standing surface waves can the subsolar magnetopause support? *Journal of Geophysical Research: Space Physics*, 120(5):3632–3646, 2015.
- [20] A. J. Ridley, T. I. Gombosi, and D. L. DeZeeuw. Ionospheric control of the magnetosphere: Conductance. *Annales Geophysicae*, 22(2):567–584, 2004.
- [21] Lutz Rastätter, Gábor Tóth, Maria M. Kuznetsova, and Antti A. Pulkkinen. Calcdeltab: An efficient postprocessing tool to calculate ground-level magnetic perturbations from global magnetosphere simulations. *Space Weather*, 12(9):553–565, 2014.
- [22] W. J. HUGHES and D. J. SOUTHWOOD. Effect of atmosphere and ionosphere on magnetospheric micropulsation signals. *Nature*, 248(5448):493–495, 1974.
- [23] Margaret G. Kivelson and David J. Southwood. Hydromagnetic waves and the ionosphere. *Geophysical Research Letters*, 15(11):1271–1274, 1988.
- [24] M. O. Archer. World’s largest drum discovered... in space. <https://www.youtube.com/watch?v=p68OmERKy4M>, Feb 2019.
- [25] W. Lotko. Inductive magnetosphere-ionosphere coupling. *Journal of Atmospheric and Solar-Terrestrial Physics*, 66(15-16):1443–1456, 2004.
- [26] C. A. Feltman. Distribution of hall and pedersen current closure in the ionosphere-magnetosphere coupling region. *The University of Iowa*.



- [27] J. W. Gjerloev. A global ground-based magnetometer initiative. *Eos, Transactions American Geophysical Union*, 90(27):230, 2009.
- [28] K.H. Glassmeier, H. Volpers, and W. Baumjohann. Ionospheric joule dissipation as a damping mechanism for high latitude ulf pulsations: Observational evidence. *Planetary and Space Science*, 32(11):1463–1466, 1984.
- [29] M. Lockwood. Identifying the open-closed field line boundary. *Polar Cap Boundary Phenomena*, page 73–90, 1998.